Dalton Transactions

Accepted Manuscript

ROYAL SOCIETY OF CHEMISTRY

www.rsc.org/dalton

Cite this: DOI: 10.1039/c0xx00000x

www.rsc.org/xxxxxx

ARTICLE TYPE

Simulated sunlight photocatalytic degradation of aqueous *p*-nitrophenol and bisphenol A in the Pt/BiOBr film-coated quartz fiber photoreactor

Yanqin Jia[b], Yuxin Yang[a], Yingna Guo[b], Wan Guo[b], Qin Qin[b], Xia Yang[a,*], Yihang Guo[a,*]

Received (in XXX, XXX) Xth XXXXXXXXX 20XX, Accepted Xth XXXXXXXXX 20XX

DOI: 10.1039/b000000x

Pt/BiOBr film-coated quartz fiber bundles were prepared by dip-coating combined with photodeposition, and their phase and chemical structures, electronic and optical properties, textural properties as well as morphologies were well-characterized. The simulated sunlight photocatalytic performance including activity and stability of as-prepared Pt/BiOBr film was evaluated in a self-made quartz fiber photoreactor by selecting two typical light-insensitive organic pollutants, *p*-nitrophenol (PNP) and bisphenol A (BPA), as the target compounds. Since the quartz fiber bundles served as both the support of Pt/BiOBr film and the medium of light propagation, Pt/BiOBr film-coated quartz fiber bundles exhibited excellent photocatalytic activity due to the enhanced light harvest ability. Additionally, the enhanced photocatalytic activity of Pt/BiOBr film was explained based on the results of photoelectrochemistry and free radicals and holes scavenging experiments.

1. Introduction

Semiconductor photocatalysis driven by solar light has great potential to eliminate organic pollutants in air and water rapidly, economically, and in an environmentally friendly manner.[1–3] However, from the viewpoint of practical application of photocatalytic technique for environment remediation, most of the reported photocatalytic systems are inappropriate due to drawbacks of limited activity and reduced sensitivity to sunlight, which result in low photocatalytic efficiency for organic removal.[4] The discovery and development of solar or visible light-responsive photocatalysts are therefore one of the essential ways to improve the photocatalytic efficiency. The other effective route is to design novel photoreactor with enhanced light harvest ability. In the search for new photocatalytic materials that may overcome the above limitations, the modified TiO_2[5–7] and TiO_2-alternative photocatalysts[8–11] have been developed. Typical and successful systems include metal or non-metal doping and heterostructuring design of integrated multi-semiconductor systems based on TiO_2; additionally, metal oxides with d^{10} main group elements (*e.g.* Bi_2O_3, In_2O_3, Ga_2O_3 or BiOX with X = Cl, Br or I) and complex metal oxides containing the cations of d^0 or d^{10} electronic configurations (*e.g.* vanadates, niobates, tungstates, titanates, tantalates and germanates) are also the promising photocatalyst candidates.[12–17] On the other hand, although the conventional slurry photoreactors can achieve high catalyst loading, they are confined to the laboratory scale for wastewater treatment because of low light utilization efficiency and difficulty in separation of photocatalyst nanoparticles from the reaction medium. Therefore, it is urgent to design the immobilized photocatalytic systems that can enhance light utilization efficiency and avoid catalyst separation step. More recently, the photocatalyst film-coated quartz fiber photoreactors have been designed, showing the enhanced photocatalytic activity in comparison of the traditional photoreactors.[18–20] The quartz fiber photoreactor that consists of numerous parallel quartz fibers for both catalyst support and light transmission has attracted special interest. The unique light propagation manner of quartz fibers makes the light reach the surface of the coated photocatalyst films directly rather than go through the reaction medium, therefore the light loss deriving from liquid absorption and photocatalyst particles scattering can be avoided. Compared with the traditional slurry systems and other catalyst-fixed photoreactors, the quartz fiber photoreactor can bring about the enhanced light utilization efficiency.

Bismuth oxyhalides (*i.e.* BiOX) belong to the family of main group multicomponent V–VI–VII semiconductor compounds, and they are the important TiO_2-alternative photocatalysts that attract considerable attention due to their excellent UV- or visible-light photocatalytic activity.[21–23] BiOX compounds are characterized by the layered structure in which halogen atoms are situated between tetragonal $[Bi_2O_2]$ layers to form $[Bi_2O_2X_2]$ layers.[24] This intrinsic plate structure endows BiOX with unique electrical, optical and catalytic activity. Moreover, the formed internal electric fields between the $[Bi_2O_2]^{2+}$ positive layers and the X^- negative layers are believed to induce an efficient separation of photogenerated electrons (e_{CB}^-) and holes (h_{VB}^+), resulting in excellent photocatalytic activity of bismuth oxyhalides.[25,26] Among various bismuth oxyhalides, BiOBr is of particular importance because of its visible light responsive (bandgap of 2.8 eV),[27,28] and relatively stable under light irradiation.[24] However, it is still necessary to further improve its photocatalytic efficiency. For this purpose, various modified BiOBr photocatalysts prepared by doping, coupling and

supporting have emerged.[29–31]

On the basis of our previous studies, Pt/BiOBr film-coated quartz fiber bundles were prepared in the present work. The simulated sunlight photocatalytic performance of Pt/BiOBr film was evaluated by selecting *p*-nitrophenol (PNP) and bisphenol A (BPA) as the target compounds. By the combination of localized surface plasmon resonance (LSPR) effect and electron-sink function of Pt nanoparticles with unique optical propagation of quartz fibers, the simulated sunlight photocatalytic activity of BiOBr is expected to be improved through facilitating the transportation and separation of the photogenerated carriers and utilizing solar spectrum more effectively. Additionally, the mechanism of photocatalytic degradation of aqueous organic pollutants over the Pt/BiOBr was revealed based on the results of photoelectrochemistry experiments and active species scavenging experiments.

2. Experimental

2.1. Preparation of Pt/BiOBr powder or film

2.1.1. BiOBr powder

$Bi(NO_3)_3$•$5H_2O$ (2 mmol) was added into ethanol (10 mL) under vigorous stirring for 0.5 h. Meanwhile, cetyltrimethylammonium bromide (CTAB, 2 mmol) was dissolved in distilled water (20 mL). The obtained CTAB solution was added dropwise into the above $Bi(NO_3)_3$ solution. After being stirred for another 0.5 h, the resulting suspension was transferred into a Teflon-lined stainless steel autoclave and heated to 160 ^oC with a heating ramp of 2 ^oC min^{-1} for 24 h, and then the autoclave was cooled down naturally. The resulting white solid precipitate was washed thoroughly with distilled water and ethanol to remove any possible impurities. Finally, the product was dried at 80 ^oC for 12 h.

2.1.2. Pt/BiOBr powder

As-prepared BiOBr powder (0.6 g) was dispersed into an aqueous solution (50 mL) containing various amount (0.05, 0.11, 0.27, 0.54, 1.1 and 2.8 mL, respectively) of H_2PtCl_6•$6H_2O$ (30 mg mL^{-1}) to obtain Pt/BiOBr powders with various Pt loadings. The resulting suspension was irradiated by a 300 W Xe lamp (PLS-SXE300, Beijing Trusttech Co., Ltd., China) for 2 h under magnetic stirring. The separated powder was washed with distilled water and ethanol three times, and then it was dried at 80 ^oC for 12 h. The product was denoted as Pt/BiOBr-x, where x refers to the determined Pt loading (%) in the Pt/BiOBr powder. Herein, x was determined by a Leeman Prodigy Spec ICP-AES, and they were 0.11, 0.27, 0.43, 1.11, 1.99 and 3.94%, respectively; moreover, the determined x values were consistence with those of the expected.

2.1.3. BiOBr suspension

Tetraethyl orthosilicate (5 mL) was dissolved into ethanol (2.6 mL) under vigorous stirring for 30 min, and then HCl (0.7 mol L^{-1}, 1.7 mL) was added, followed by refluxing under atmosphere (78 ^oC) for 50 min. Subsequently, an appropriate amount of BiOBr (2.5 g) was completely dispersed into the mixture of ethanol (30 mL) and freshly prepared silica sol (1 mL). The resulting mixture was stirred for 1 h. The formed uniform and adherent BiOBr suspension was used for quartz fiber coating.

2.1.4. BiOBr film-coated quartz fiber bundles

The clear quartz fiber bundles (80 mm length each, diameter 0.6 mm) were dipped into the freshly prepared BiOBr suspension and kept for 2 min, and then they were withdrawn slowly. After being dried for 30 min at room temperature, the dip-withdrawn procedure was repeated to obtain the film with different layers. The BiOBr film-coated quartz fiber bundles were heated at 40 ^oC for 2 h, 60 ^oC and 80 ^oC for 1 h, and then they were washed with water and dried at 80 ^oC. The product was denoted as BiOBr (yL), where y referred to number of layer of BiOBr film. Herein, y =3, 5 and 7.

2.1.5. Pt/BiOBr film-coated quartz fiber bundles

Each BiOBr film-coated quartz fiber bundle was inserted vertically into the hole of self-made Teflon plate (in which 301 holes were distributed). The fixed quartz fiber bundles were immersed into 270 mL aqueous H_2PtCl_6•$6H_2O$ (1.28 or 2.56 μg mL^{-1}) solution. The system was irradiated by Xe lamp for 2 h to obtain Pt/BiOBr film-coated quartz fiber bundles, and then the bundles were washed with water and ethanol successively. After being dried at 80 ^oC, Pt/BiOBr (yL)-z film was obtained, where z represented Pt loading (%) in the Pt/BiOBr film. Herein, z = 0.13, 0.22 and 2.10%, respectively.

2.2. Characterization of Pt/BiOBr powder or film

XRD patterns were recorded by a Japan Rigaku D/max 2000 X-ray diffractometer (Cu Kα, λ = 1.5418 Å). UV-Vis diffuse reflectance spectra (UV-Vis/DRS) were carried out by a Cary 500 UV-Vis-NIR spectrophotometer. X-ray photoelectron spectra (XPS) were investigated on a VG-ADES 400 instrument with Mg K-ADES source at a residual gas pressure of below 10−8 Pa. Field emission scanning electron microscope (FESEM, XL-30 ESEM FEG) and transmission electron microscope (TEM, JEM-2100F) were employed to observe the morphology of the samples. Nitrogen gas porosimetry measurement was obtained using a Micromeritics ASAP 2020M surface area and porosity analyzer.

2.3. Photocatalytic tests

Simulated sunlight irradiation was provided by a 300 W Xe lamp equipped with an IR cut filter. For adsorption and photocatalytic tests of the powder photocatalyst, 100 mg catalyst was dispersed into 100 mL PNP solution (10 mg L^{-1}). Before irradiation, the suspension was ultrasonicated for 10 min and then stirred in the dark for 60 min to obtain the adsorption-desorption equilibrium between PNP molecules and the catalyst. At given intervals of irradiation, the sample solution was withdrawn and followed by centrifugation. The concentrations of PNP were analyzed using a Cary 60 UV-Vis spectrophotometer at 317 nm. For the film photocatalyst, the fixed 224 pieces of quartz fiber bundles were placed vertically into the quartz reactor (Fig. S1 of ESI). The initial concentration of PNP or BPA is 5 mg L^{-1}, and the solution volume is 270 mL. Before light irradiation, the quartz fiber bundles were soaked in the reaction solution for 1 h to establish an adsorption-desorption equilibrium. The concentrations of BPA were monitored by an Agilent 1200 HPLC: C_{18} column, UV detector (λ = 281 nm), methanol/water (75/25, v/v, 0.8 mL min^{-1}).

2.4. Photoelectrochemical experiments

The working electrode was prepared on the rectangle titanium (Ti) sheets (size 10 × 50 mm^2, thickness 140 μm, purity > 99.6%), which was cleaned by sonication in water and ethanol for 10 min, respectively. The cleaned Ti sheets were chemically etched in a mixture of HF, HNO_3 and H_2O for 30 s (HF: HNO_3: H_2O = 1: 4:

5; v/v/v) followed by rinsing with distilled water and placed in alcohol. The catalyst powder (10 mg) was mixed with ethanol (2 mL) under sonication for 10 min to get slurry. The obtained slurry was used for spin-coating on the Ti sheet at an initial spin rate of 500 rpm for 9 s and then 2000 rpm for 10 s. After aging at room temperature for 24 h, BiOBr and Pt/BiOBr covered Ti sheets were washed with distilled water three times. Finally, the coated Ti sheets were dried at 60 ^{o}C for 12 h.

The experiments were conducted in an electrochemical analyzer (CHI 630E, Shanghai Chenhua, China) with a standard three-electrode system (the prepared photocatalyst/Ti sheet, Pt wire and Ag/AgCl were used as the working electrode, counter electrode and reference electrode, respectively). Xe lamp was used as the light source, and Na_2SO_4 aqueous solution (0.01 mol L^{-1}, 110 mL) was served as the electrolyte.

3. Results and discussion

3.1. Preparation and characterization of Pt/BiOBr powder or film

The key step to prepare BiOBr film-coated quartz fiber bundles is to obtain uniform BiOBr suspension with suitable viscosity, and therefore, the preparation conditions including BiOBr powder-to-EtOH-to-silica sol weight ratio and stirring time should be controlled carefully. Subsequently, the nude quartz fiber bundles are dipped into the freshly prepared BiOBr suspension to obtain BiOBr film-coated quartz fiber bundles by dipping-withdrawing. As for Pt/BiOBr film-coated quartz fiber bundles, they are easily fabricated by immersing the BiOBr film-coated quartz fiber bundles into H_2PtCl_6•$6H_2O$ solution under simulated sunlight irradiation.

3.1.1. Structural information

The phase structure of as-prepared BiOBr-based powder samples are investigated by XRD analysis (Fig. 1). For pure BiOBr sample, it shows tetragonal crystal phase with the detected reflections at 10.9 (001), 21.9 (002), 25.2 (101), 31.7 (102), 32.2 (110), 33.1 (003) and 50.7° (104), respectively (JCPDS 78-0348); meanwhile, the intense and sharp diffraction peaks imply the high crystallinity of BiOBr. It is also found that the (102) facet is dominantly exposed for BiOBr. After Pt particles deposited on the BiOBr nanoplates, the diffractions corresponding to tetragonal crystal phase can also be found for three representative Pt/BiOBr samples, *i.e.* Pt/BiOBr-0.27, Pt/BiOBr-1.99 and Pt/BiOBr-3.94; meanwhile, these samples possess the most intense peak of (001) crystal facet, regardless of Pt loading levels. The result suggests that BiOBr nanoplates favor to grow along (001) crystal facet in the presence of Pt particles. However, no diffraction peaks indexed to the crystal reflections of metallic Pt phase are found, probably due to low Pt loading level, small particle size of Pt as well as uniform distribution of Pt particles throughout the layered BiOBr nanoplates.

XPS surface probe technique is applied to confirm the existence of metallic Pt particles in the Pt/BiOBr sample. As shown in Fig. S2 of ESI, the peaks of Pt $4f_{7/2}$ and Pt $4f_{5/2}$ for Pt/BiOBr-1.99 sample appear at 71.2 and 74.4 eV, and the corresponding spin energy separation is 3.2 eV. This is the characteristic of metallic Pt, suggesting that Pt exists as a metallic state in the Pt/BiOBr materials.[32]

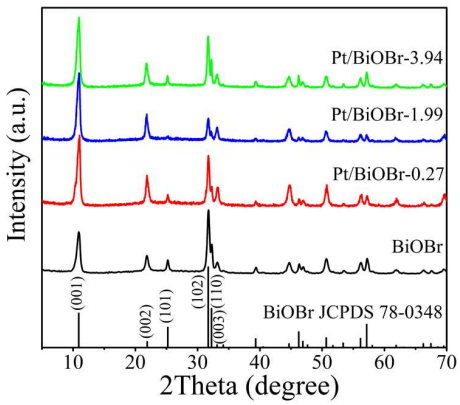

Fig. 1. XRD patterns of the BiOBr-based powder samples.

3.1.2. Morphology

Morphologies of as-prepared BiOBr-based powder or film samples are revealed by TEM (Fig. 2) and FESEM (Fig. 3) observations. Fig. 2a presents the TEM image of BiOBr powder, showing that it consists of numerous transparent thin plates growing in various directions. Fig. 2b-d display the TEM images of Pt/BiOBr-1.11, Pt/BiOBr-1.99 and Pt/BiOBr-3.94 powder, respectively. Different from pure BiOBr, Pt/BiOBr mainly shows single-direction growth. In addition, at lower Pt loading (1.11 and 1.99%), tiny and spherical Pt particles with average diameter of 5–10 nm homogeneously dispersed on the surface of BiOBr nanoplates (Fig. 2b and c). As increasing Pt loading to 3.94%, Pt clusters are observed on the surface of BiOBr, attributing to the aggregation of Pt nanoparticles (Fig. 2d).

In line with TEM observation, the panoramic view shown in FESEM image also indicates that BiOBr powder is composed of randomly organized nanoplates with the thickness of *ca.* 45 nm (Fig. 3a). CTAB can function not only as Br source but also as the template that is responsible for the formation of plate-like BiOBr.[33] In the case of Pt/BiOBr-1.99 powder, the plate-like BiOBr morphology remains intact, but BiOBr with single-direction crystal growth is observed (Fig. 3b). This may be due to the existence of Pt nanoparticles can affect the facet growth direction. From Fig. 3b it is also observed that spherical Pt nanoparticles homogeneously dispersed on the surface of BiOBr nanoplates. Fig. 3c and d display the FESEM images of Pt/BiOBr (7L)-0.22 film-coated quartz fibers, and the estimated film thickness is *ca.* 750 nm. Moreover, the film still exhibits irregular plate-like morphology. This may be due to the fact that low content of Pt particles cannot affect the facet growth direction of BiOBr. Additionally, Pt particles are hardly observed from FESEM observation, probably due to its low content (0.22%).

3.1.3. Textural property

The textural properties of as-prepared BiOBr-based films were studied by nitrogen gas porosimetry measurement, and the selected representative samples include BiOBr (7L), Pt/BiOBr (7L)-0.13 and Pt/BiOBr (7L)-0.22 film. From Fig. S3 of ESI it is found three tested film materials exhibit type IV adsorption-desorption isotherms with H3-type hysteresis loop, and the capillary condensation steps occur at relative pressure (P/P_0) of 0.95–1.0. The result suggests that both BiOBr and Pt/BiOBr films exhibit mesoporosity, and their mesoporosity is contributed from the voids between BiOBr nanoplates. The calculated BET surface

areas of BiOBr (7L), Pt/BiOBr (7L)-0.13 and Pt/BiOBr (7L)-0.22 film based on the above nitrogen gas adsorption-desorption isotherms are 6.7, 11.1 and 21.6 m^2 g^{-1}, respectively. The increased BET surface area of Pt/BiOBr film in comparison of BiOBr film is due to homogeneously dispersed tiny Pt nanoparticles on the BiOBr nanoplates.

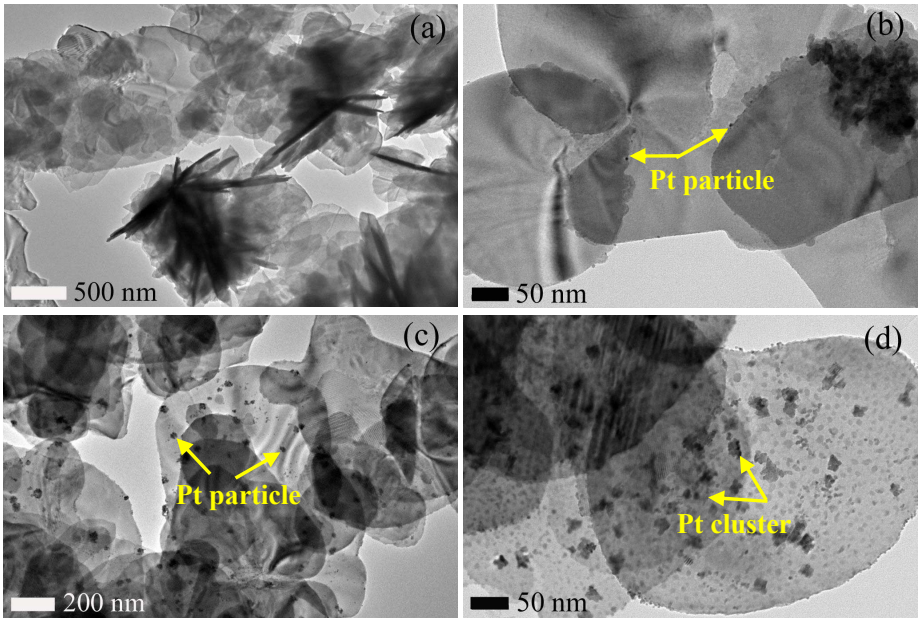

Fig. 2. TEM images of powder samples. BiOBr (a), Pt/BiOBr-1.11 (b), Pt/BiOBr-1.99 (c) and Pt/BiOBr-3.94 (d).

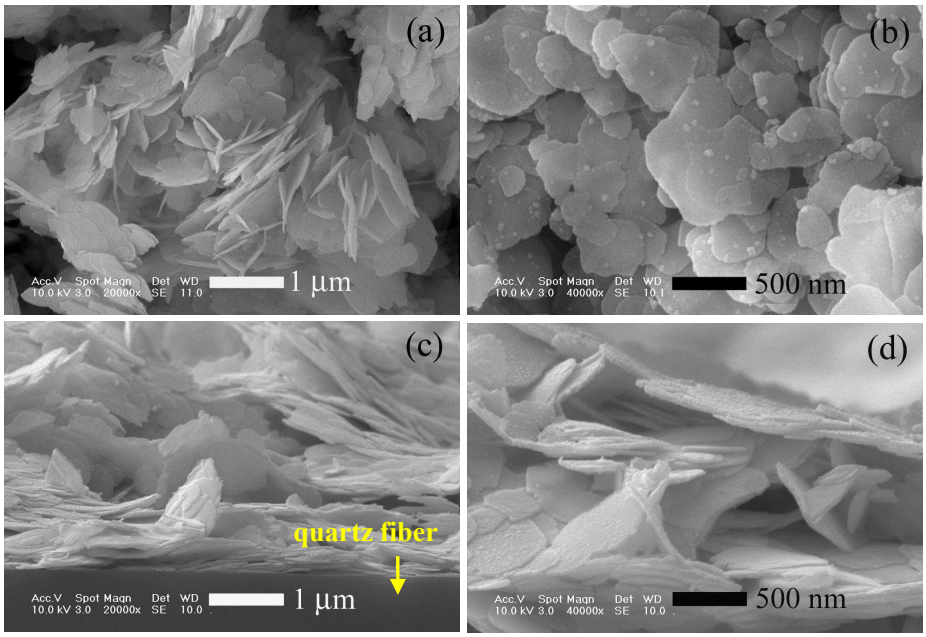

Fig. 3. FESEM images of BiOBr powder (a), Pt/BiOBr-1.99 powder (b) and Pt/BiOBr (7L)-0.22 film-coated quartz fiber bundles (c and d).

3.1.4. Optical absorption property

The optical absorption properties of the photocatalysts are important issues to dominate their catalytic activity since all the photochemical processes are initiated by light absorption. In the present work, the optical absorption properties of BiOBr and Pt/BiOBr films are studied by UV-vis/DRS (Fig. 4). Fig. 4a displays the normalized UV-Vis/DRS of as-prepared BiOBr films with different thicknesses (*i.e.* 3, 5 and 7 layers). It shows that each BiOBr film has absorption edge ending up to *ca*. 430 nm, which is attributed to electron transition from the valence band (hybridized O 2*p* and Br 4*p* orbital) to the conduction band (Bi 6*p* orbital).[34] Moreover, with the number of BiOBr layers increasing from 3, 5 to 7, the absorbance of the film increases gradually, suggesting the increased weight of BiOBr film. After the deposition of Pt nanoparticles within BiOBr layered structure, the

absorption edge has somewhat redshift, accompanying with new and weak absorptions in the visible light region (430–800 nm, Fig. 4b). The optical absorption of the Pt/BiOBr films produced in the visible light region is mainly originates from the LSPR effect of metallic Pt nanoparticles[35]; additionally, the light scattering effect due to Pt particles can also contribute to the visible light absorptions.[36] In addition, gradually increased absorption intensity of the films with Pt loading from 0.13, 0.22 to 2.10% implies the enhanced LSPR effect of metallic Pt.

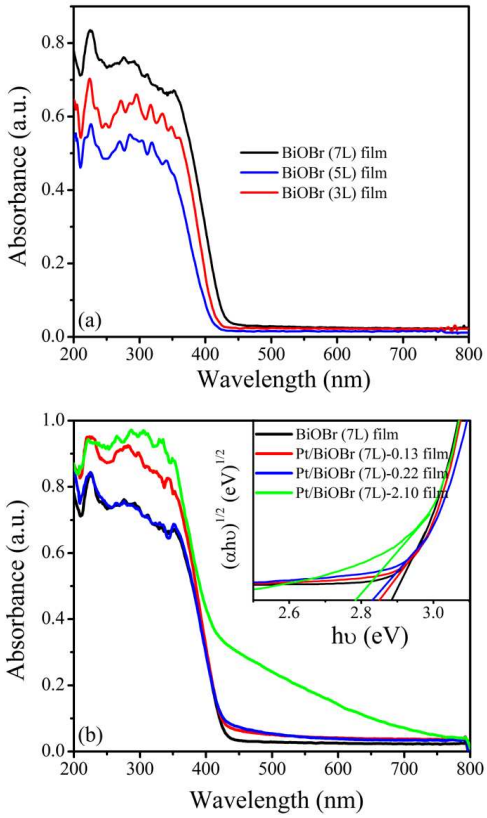

Fig. 4. UV-Vis/DRS of (a) BiOBr films with different thicknesses, and (b) Pt/BiOBr films with different Pt loading levels. Inset of (b) is the plots of $(\alpha h\nu)^{1/2}$ *vs.* hν.

For a crystalline semiconductor, the optical absorption near the absorption edge follows Kubelka-Munk formula

$$\alpha h\nu = A\,(h\nu - E_g)^{n/2}$$

where α, ν, E_g and A are absorption coefficient, light frequency, band gap energy, and a constant, respectively.[37] As for n, it is determined by the type of optical transition of a semiconductor (n = 1 for direct transition and n = 4 for indirect transition). The value of n for BiOBr is 4. Therefore, E_g of BiOBr (7L) film, Pt/BiOBr(7L)-0.13, Pt/BiOBr(7L)-0.22 and Pt/BiOBr(7L)-2.10 film are estimated from the plot of $(\alpha h\nu)^{1/2}$ *vs.* hν (Inset of Fig. 4b), and they are 2.88, 2.85, 2.82 and 2.77 eV, respectively.

3.2. Photocatalytic tests

3.2.1. Photocatalytic activity of Pt/BiOBr powders

The photocatalytic activity of Pt/BiOBr powders with different Pt loadings is evaluated firstly to find out the influence of Pt loading on the photocatalytic activity, and therefore, the optimal Pt loading is confirmed for subsequent preparation of Pt/BiOBr film-coated quartz fiber bundles. In order to exclude the photosensitized effect and obtain a real photocatalytic activity in the BiOBr- or Pt/BiOBr-catalyzed organic pollutant degradation process, light-insensitive PNP is selected as the target compound.

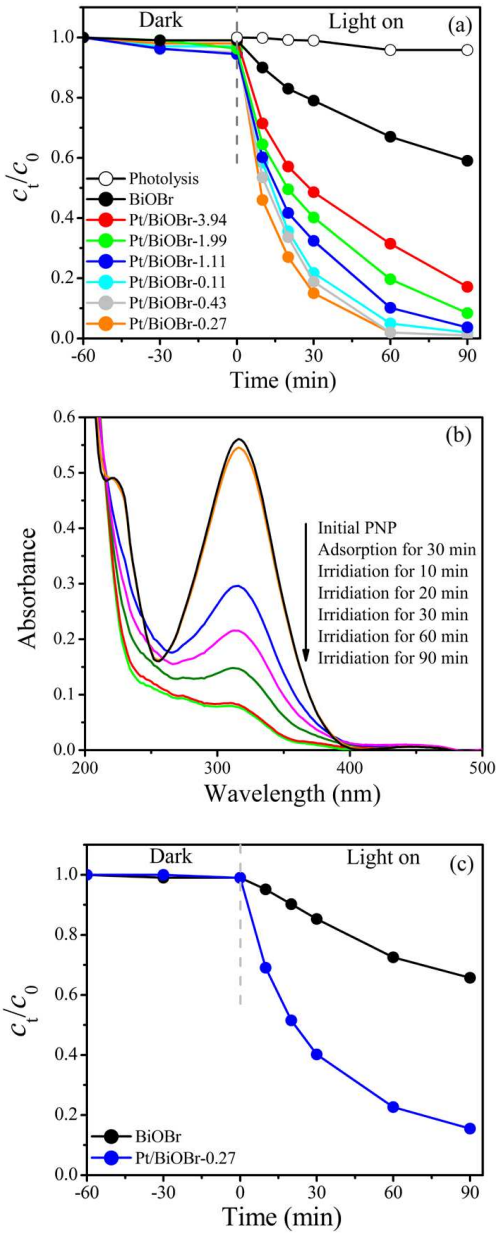

Fig. 5. (a) Adsorption property and photocatalytic activity of BiOBr-based powders toward the degradation of PNP under simulated sunlight irradiation (320 nm < λ < 680 nm); (b) UV-vis absorption spectra of PNP as a function of irradiation time during the degradation process catalyzed by Pt/BiOBr-0.27 powder. (c) Adsorption property and photocatalytic activity of BiOBr-based powders toward the degradation of PNP under visible light irradiation (420 nm < λ < 680 nm). c_0 = 10 mg L^{-1}; volume 100 mL; catalyst amount 100 mg.

From the result displayed in Fig. 5a it is found that adsorption of PNP molecules on BiOBr powder can be ignored; additionally, the adsorption capacity of Pt/BiOBr powder to PNP molecules increases slightly, regardless of Pt loadings. Direct simulated sunlight (320 nm < λ < 680 nm) photolysis shows the degradation of PNP hardly occurs. However, significant degradation of PNP

happens in the presence of both photocatalyst and simulated sunlight irradiation. Moreover, Pt/BiOBr powder shows obviously higher photocatalytic activity than pure BiOBr powder, and the photocatalytic activity of Pt/BiOBr powder is closely related to Pt loading. Pt/BiOBr powders with lower Pt loading (*e.g.* 0.11 and 0.27%) show relatively higher photocatalytic activity toward PNP degradation than Pt/BiOBr powders with higher Pt loading (*e.g.* 0.43, 1.11, 1.99 and 3.94%). For example, after simulated sunlight irradiation for 60 min, the conversion of PNP reaches to 33.0 (BiOBr), 68.6 (Pt/BiOBr-3.94), 80.4 (Pt/BiOBr-1.99), 90.0 (Pt/BiOBr-1.11), 95.5 (Pt/BiOBr-0.43), 98.0 (Pt/BiOBr-0.27) and 98.0% (Pt/BiOBr-0.11), respectively. Considering high efficiency and low price, Pt loading is controlled in the range from 0.11 to 0.27% for subsequent preparation of Pt/BiOBr film coated quartz fiber bundles.

Fig. 5b shows the variations of the characteristic absorption of PNP under simulated sunlight irradiating the most photoactive Pt/BiOBr-0.27. The absorption of PNP reduces gradually with prolonging the irradiation time, and the absorption is hardly observed after 90 min simulated light irradiation. The result is in line with Fig. 5a.

The visible light (420 nm < λ < 680 nm) photocatalytic activity of BiOBr and Pt/BiOBr-0.27 powder toward the degradation of PNP is presented in Fig. 5c. It shows Pt/BiOBr-0.27 powder still exhibits considerably higher visible light photocatalytic activity with respect to BiOBr. For example, the conversion of PNP reaches to 85.3 and 35.0%, respectively, after visible light irradiating Pt/BiOBr-0.27 and BiOBr for 90 min. The result implies LSPR effect of Pt nanoparticles has a positive influence on the photocatalytic activity of BiOBr.

3.2.2. Photocatalytic activity of Pt/BiOBr film-coated quartz fiber bundles

Our previous work shows that compared with photocatalyst film-coated quartz fiber bundles placed horizontally, the vertical configuration is favorable to improve light utilization efficiency.[19] In this mode, quartz fibers are not only the catalyst support but also the light transmitter. Accordingly, light loss from liquid absorption can be reduced since the light reach to the photocatalyst film coated quartz fiber surface directly rather than passing through the reaction media. Light scattering from catalyst particles can also be avoided due to the unique light propagation manner. The light split two parts once emitting from Xe lamp and reaching to the interface between quartz core of quartz fiber and the coated film photocatalyst. One part of light is refracted to the photocatalyst particles film and then absorbed by them, the other part transmits along the quartz fibers by reflection (Fig. S4 of ESI).[19] This process occurs repeatedly, leading to the enhanced light utilization efficiency.

At first, the influence of the thickness of the film on the photocatalytic activity is studied by selecting BiOBr (3L) film, BiOBr (5L) film and BiOBr (7L) film as the representative film photocatalysts and BPA as the target compound. From the result shown in Fig. 6a it is found that: i) only 10% of BPA is degraded by direct simulated sunlight irradiation; ii) increasing the thickness of the BiOBr film from 3, 5 to 7 layers, the adsorption capacity to BPA molecules increases gradually; and iii) obvious degradation of BPA is observed after simulated sunlight irradiating the BiOBr films, and the photocatalytic activity of the BiOBr film gradually enhances as increasing the thickness of the film from 3, 5 to 7 layers, attributing to gradually increased BiOBr film weight (45, 90 and 130 mg for 3, 5 and 7 layers, respectively) and light harvest ability. Further increasing BiOBr film thickness may lead to much higher photocatalytic activity, however, obvious drop of BiOBr film from quartz fiber bundles into the reaction media has been found. On the other hand, too thin film (*e.g.* 1 layer or 2 layers) not only leads to less BiOBr film weight but also reduces the light utilization. Both of these factors can limit the photocatalytic activity. Therefore, the optimum film thickness of BiOBr-based films is controlled at 7 layers in the present work. At the film thickness of 7 layers, the photocatalytic activity of the Pt/BiOBr (7L)-0.22 film toward the degradation of BPA is also tested, showing that it is more photoactive than BiOBr (7L) film. After 90 min simulated sunlight irradiation, the conversion of BPA reaches to 70% [BiOBr (7L) film] and 100% [Pt/BiOBr (7L)-0.22 film], respectively (Fig. 6a).

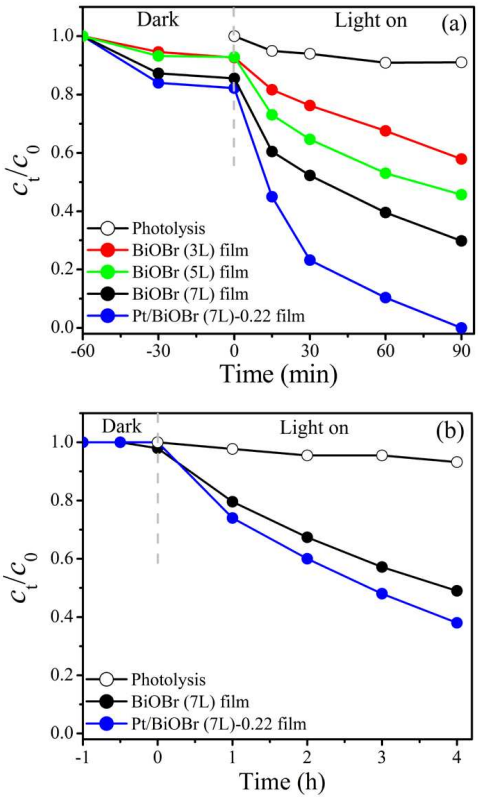

Fig. 6. (a) Adsorption property and photocatalytic activity of various BiOBr-based films-coated quartz fiber bundles toward the degradation of BPA; and (b) adsorption property and photocatalytic activity of BiOBr (7L) film- and Pt/BiOBr (7L)-0.22 film-coated quartz fiber bundles toward the degradation of PNP. Simulated sunlight irradiation (320 nm < λ < 680 nm); c_0 (PNP and BPA) = 5 mg L^{-1}; volume 270 mL; catalyst amount 45 mg (3 layers), 90 mg (5 layers), 130 mg (7 layers).

Subsequently, the adsorption property and photocatalytic activity of BiOBr (7L) film- and Pt/BiOBr (7L)-0.22 film-coated quartz fiber bundles are further tested by selecting PNP as the target compound. From the result shown in Fig. 6b it can be seen that the photocatalyst films show very weak adsorption to PNP molecules, while direct photolysis can hardly change the concentration of PNP. In the presence of both photocatalyst film and simulated sunlight irradiation, Pt/BiOBr (7L)-0.22 film

exhibits higher photocatalytic activity compared with BiOBr (7L) film. The conversion of PNP is 62% [Pt/BiOBr (7L)-0.22 film] and 52% [BiOBr (7L) film] after simulated sunlight irradiation for 4 h.

The difference of the degradation rate between PNP and BPA is due to their different chemical structures. In the process of photocatalytic degradation of an aqueous BPA over BiOBr-based photocatalysts, the ring opening can directly happen because of its highly symmetrical structure, and then the formed intermediates suffer from further degradation to CO_2 and H_2O.[38] However, in the process of photocatalytic degradation of an aqueous PNP, a series of steps happen. Firstly, PNP is photooxidized into hydroquinone, hydroquinone is further photooxidized to benzoquinone, and then the ring opening reaction happens gradually to form 2-butenedioic acid, acetic acid, formic acid and oxalic acid. Continuous degradation of the above intermediates leads to final products such as CO_2 and H_2O.[39] Accordingly, the degradation rate of BPA is faster than PNP over the same photocatalyst.

3.2.3. Regeneration and reusability of Pt/BiOBr film-coated quartz fiber bundles

For practical photocatalytic applications of the supported photocatalyst film in aqueous solution, recycling is a difficult task owing to drops of the films from the supports. Regeneration and reusability of Pt/BiOBr (7L)-0.22 film is investigated through the photocatalytic degradation of BPA. After each recycling run, Pt/BiOBr (7L)-0.22 film is washed with 1% (v/v) H_2O_2 under simulated sunlight irradiation to remove all residual intermediates; subsequently, the films are washed with ethanol. The deactivation of the film catalyst is hardly occurred after five consecutive runs (Fig. 7), indicating that the prepared Pt/BiOBr film is photocatalytically stable enough. Meanwhile, the leaching of Pt into the reaction solution after each catalytic run can be neglected (the determined Pt is below the detect limit of ICP-AES). The high photocatalytic stability of Pt/BiOBr film is due to enough adherence of the films on quartz fiber bundles. By the combination of high catalytic efficiency, no separation step and excellent reusability, Pt/BiOBr film-coated quartz fiber bundles are regarded as promising supported photocatalysts that may find practical applications for removal aqueous organic pollutants.

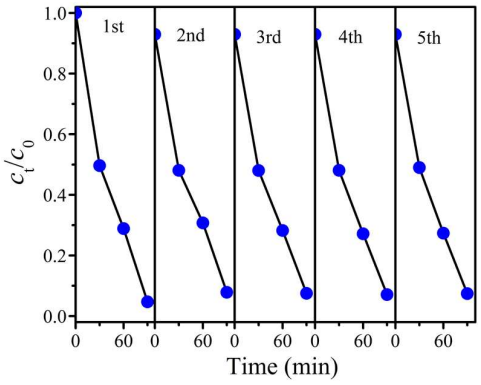

Fig. 7. Recycling experiments of Pt/BiOBr (7L)-0.22 film-coated quartz fiber bundles toward the degradation of BPA. Simulated sunlight irradiation (320 nm < λ < 680 nm); c_0 (BPA) = 5 mg L^{-1}; volume 270 mL; catalyst amount 130 mg.

3.3 Mechanism considerations

3.3.1. Photoelectrochemical experiments

Photoelectrochemistry experiments are carried out to monitor the generation of photoexcited electrons and holes as well as their separation and migration in BiOBr and Pt/BiOBr system. From the photocurrent-time (*I-t*) curves displayed in Fig. 8 it is found that the photocurrent responses of the tested BiOBr-based working electrodes decrease to zero rapidly once Xe lamp is turned off; meanwhile, the photocurrent responses retain the reproducible value as soon as Xe lamp is turned on again during three on-off intermittent irradiation cycles. Three tested Pt/BiOBr materials with Pt loading of 0.27, 1.11 and 1.99% exhibit higher photocurrent responses with respect to BiOBr. Interestingly, Pt/BiOBr-0.27 shows the highest photocurrent intensity that is 1.8 times higher than BiOBr, and the photocurrent intensity gradually weakens as increasing Pt loading to 1.11 and 1.99%. The sequence of the photocurrent intensities is consistent with the order of the photocatalytic activity of BiOBr-based materials. It should be mentioned that the photocurrent response of pure Ti sheet can be neglected since very small photocurrent (lower than 1×10^{-6} A) is detected in this system. The result confirms that the Ti sheets used herein are clean and without impurity after chemically etching in a mixture of HF, HNO_3 and H_2O.

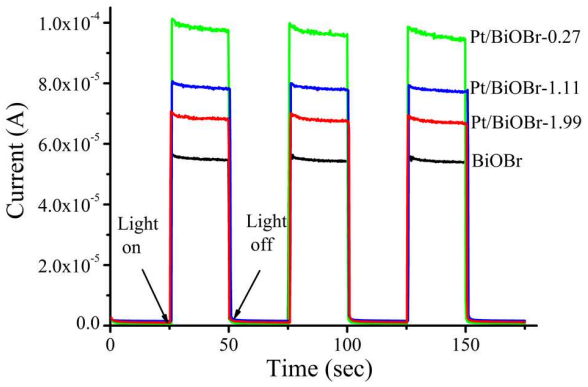

Fig. 8. Photocurrent responses of BiOBr/Ti and Pt/BiOBr/Ti electrodes under simulated sunlight illumination.

The photocurrent is produced by the diffusion of e_{CB}^- to the Ti sheet. Therefore, the enhanced photocurrent response of Pt/BiOBr-0.27/Ti electrode indicates a more efficient separation of h_{VB}^+–e_{CB}^- pairs or a longer lifetime of the photogenerated charge carriers as compared to Pt/BiOBr-1.11/Ti or Pt/BiOBr-1.99/Ti electrode. Additionally, the enhanced photocurrent response of Pt/BiOBr with respect to BiOBr is due to the strong electron-accept ability of Pt nanoparticles, leading to faster separation and transportation of the e_{CB}^- on the surface of the working electrodes. However, higher Pt loading (*e.g.* 1.11 and 1.99%) in the Pt/BiOBr materials does not produce much higher photocurrent than Pt/BiOBr-0.27. This is due to the fact that the aggregation of Pt nanoparticles owing to higher Pt loading can induce new h_{VB}^+–e_{CB}^- recombination center, and thereby prohibiting further generation of h_{VB}^+ and e_{CB}^-. As a consequence, the decreased photocatalytic activity of Pt/BiOBr with higher Pt loading has been found.

3.3.2. Free radical and hole scavenging experiments

Active species generated during the process of the photodegradation of PNP over BiOBr (7L) film and Pt/BiOBr (7L)-0.22 film are identified by free radical and hole trapping experiments. Tert-butyl alcohol (*t*-BuOH), EDTA-2Na and 1, 4-benzoquinone (BQ) are used as hydroxyl radical ($^{\bullet}OH$), hole (h_{VB}^{+}) and superoxide radical ($^{\bullet}O_2^{-}$) scavenger, respectively.

In BiOBr photocatalytic system (Fig. 9a), the addition of 1mM *t*-BuOH can hardly inhibit PNP degradation. This is due to the fact that the standard redox potential of Bi^{5+}/Bi^{3+} (1.59 eV) is less positive than the $^{\bullet}OH/OH^{-}$ (+1.99 eV *vs*. NHE). Accordingly, $^{\bullet}OH$ radicals cannot be generated from oxidation of OH^{-} by h_{VB}^{+}.[40] The photocatalytic activity of BiOBr significantly decreases by the addition of 1mM BQ, demonstrating that $^{\bullet}O_2^{-}$ is one of the active species generated in the BiOBr-photocatalyzed system. Additionally, the degradation rate of PNP is obviously sped in the presence of 1mM EDTA-2Na. This is due to the fact that h_{VB}^{+} can be scavenged by EDTA-2Na, leading to more e_{CB}^{-} react with O_2 to form extra $^{\bullet}O_2^{-}$ radicals instead of the rapid recombination with h_{VB}^{+}. Therefore, $^{\bullet}O_2^{-}$ is the main active species generated in BiOBr (7L) film-photocatalyzed system that is responsible for the degradation of an aqueous PNP.

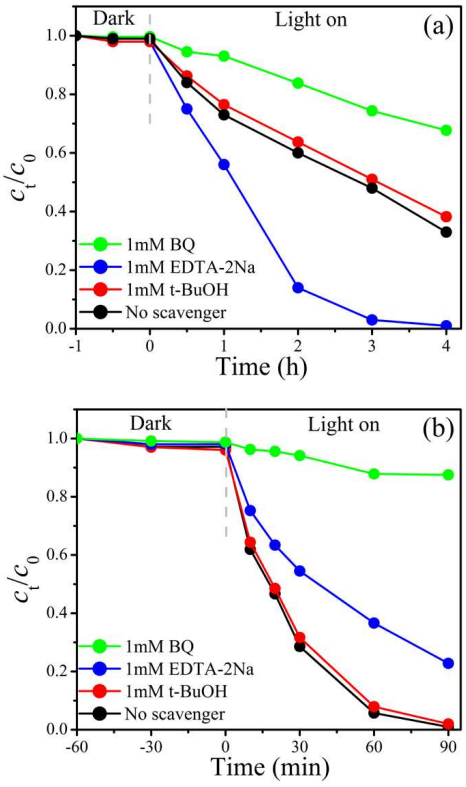

Fig. 9. Influence of various scavengers on the phohocatalytic activity of (a) BiOBr (7L) film and (b) Pt/BiOBr (7L)-0.22 film toward the degradation of PNP. Simulated sunlight irradiation (320 nm < λ < 680 nm) c_0 = 10 mg L^{-1}; volume 100 mL; catalyst amount 100 mg.

Fig. 9b shows the trapping experiment of active species generated in Pt/BiOBr (7L)-0.22 film photocatalyzed system. It can be found that $^{\bullet}O_2^{-}$ radical is still the main active species generated in current system because the photodegradation reaction is inhibited significantly in the presence of BQ. Additionally, the photodegradation rate of PNP is obviously decelerated in the presence of *t*-BuOH, suggesting that h_{VB}^{+} is another active species. Similarly, $^{\bullet}OH$ is also hardly generated in current photocatalytic system. Therefore, with the help of $^{\bullet}O_2^{-}$ and h_{VB}^{+}, PNP can be decomposed more rapidly under simulated sunlight irradiating Pt/BiOBr with respect to BiOBr.

3.3.3. Mechanism

The excellent photocatalytic activity of Pt/BiOBr is due to the combination of intrinsic photocatalytic properties of BiOBr and electron-sink function as well as LSPR effect of Pt nanoparticles. Pt/BiOBr has suitable bandgap energy (*ca.* 2.8 eV) and LSPR absorption, so it can be photoexcited under simulated sunlight or visible light irradiation. Additionally, the internal electric fields in sandwich-like crystals structure of BiOBr is considered to favor the transportation and separation of h_{VB}^{+}–e_{CB}^{-} pairs, giving a positive impact to the photocatalytic activity.[41]

Under simulated sunlight irradiating BiOBr, e_{CB}^{-} and h_{VB}^{+} are generated at the surface of BiOBr. Since the CB potential (0.23 eV *vs* NHE) of BiOBr is more positive than the standard redox potential of $O_2/^{\bullet}O_2^{-}$ (−0.046 eV *vs*. NHE), $^{\bullet}O_2^{-}$ radical cannot be generated from the reduction of O_2 by e_{CB}^{-} directly.[42] Nevertheless, under simulated sunlight irradiation, the higher energy part (the wavelength is less than 430 nm, irradiation energy is higher than 2.88 eV) of BiOBr can induce the e_{CB} being excited up to a reformed higher CB potential that is more negatively than standard redox potential of $O_2/^{\bullet}O_2^{-}$. Accordingly, $^{\bullet}O_2^{-}$ still can generate by the reduction of molecular oxygen with e_{CB}^{-} (Scheme 1a).

$$\text{Pt/BiOBr} \xrightarrow{\text{simulated sunlight}} \text{Pt/BiOBr}\,(h_{VB}^{+} + e_{CB}^{-}) \quad (1)$$

$$e_{CB}^{-} + O_2 \longrightarrow {}^{\bullet}O_2^{-} \quad (2)$$

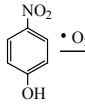

$$\xrightarrow{{}^{\bullet}O_2^{-},\ h_{VB}^{+}} NO_3^{-} + CO_2 + H_2O \quad (3)$$

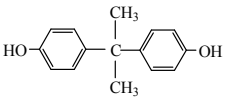

$$\xrightarrow{{}^{\bullet}O_2^{-},\ h_{VB}^{+}} CO_2 + H_2O \quad (4)$$

As for Pt/BiOBr photocatalytic system, the photogenerated e_{CB}^{-} (*Eqn*. 1) on the reformed CB of BiOBr nanoplates would transfer to Pt nanoplaticles due to the difference between CB of BiOBr and the Fermi level of Pt, resulting in fast separation of e_{CB}^{-} and h_{VB}^{+}. Meanwhile, a Schottky barrier has been created at the interface of Pt nanoparticles and BiOBr nanoplates, which minimizes the recombination of h_{VB}^{+} and e_{CB}^{-} (Scheme 1b). Accordingly, more $^{\bullet}O_2^{-}$ radicals are generated due to more e_{CB}^{-} react with dioxygen (*Eqn*. 2). The reduced recombination opportunity between h_{VB}^{+} and e_{CB}^{-} leads to enough h_{VB}^{+} are collected on the VB of BiOBr and then participate in the degradation process. Therefore, h_{VB}^{+} emerge as a new kind of active species in the Pt/BiOBr-photocatalyzed system, providing a direct evidence for the enhanced photocatalytic activity of Pt/BiOBr with respect to BiOBr. Under the assistance of h_{VB}^{+} and $^{\bullet}O_2^{-}$ radicals, PNP (*Eqn*. 3) and BPA (*Eqn*. 4) are degraded in

aqueous solution. The final product NO_3^- ion is identified by ion chromatography (Fig. S5 of ESI), while CO_2 is detected by monitoring the production of $BaCO_3$ precipitation via adding dilute $Ba(OH)_2$ solution into the reaction media.

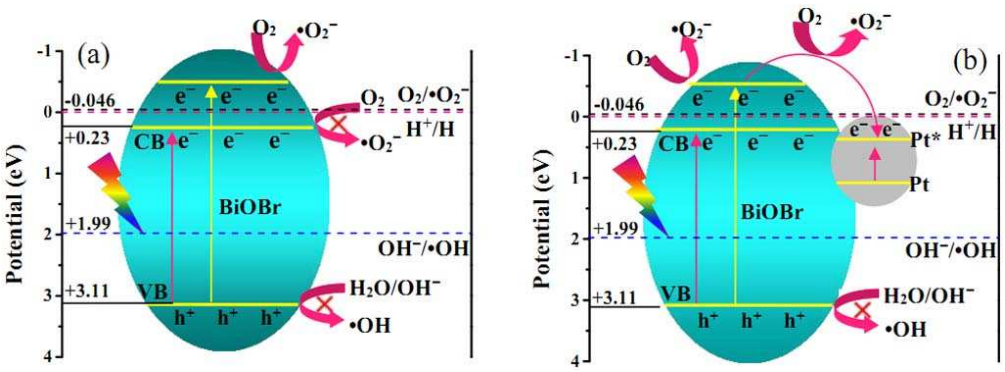

Scheme 1 Energy band diagrams of BiOBr (a) and Pt/BiOBr (b) as well as tentative process of photocatalytic degradation of an aqueous PNP over BiOBr and Pt/BiOBr.

4. Conclusions

By using a simple solvothermal route combined with dip-coating and photodeposition method, a series of Pt/BiOBr film-coated quartz fiber bundles were successfully fabricated. As-prepared Pt/BiOBr film catalysts worked effectively under simulated sunlight irradiation toward the degradation of aqueous PNP and BPA, attributing to the synergistic effect of electron-sink function and localized surface plasmon resonance effect of Pt nanoparticles as well as the unique light transmission properties of quartz fibers. Therefore, the inherent photocatalytic activity of BiOBr was significantly improved by facilitating separation and transportation of the photogenerated carriers as well as utilizing simulated sunlight more effectively. Importantly, the film photocatalyst can be reused at least five times after simple treatment of the used Pt/BiOBr film. By the combination of high catalytic efficiency, no separation step and excellent reusability, Pt/BiOBr film-coated quartz fiber bundles are regarded as a new and promising supported photocatalyst that may find practical applications for removal organic pollutants in wastewater.

Acknowledgments

This work is supported by the Natural Science Fund of China (21173036; 51278092; 51308097; 51478095). Also, the work is supported by the Program for New Century Excellent Talents in University of Ministry of Education of China (NCET-13-0723).

Notes and references

[a]*School of Environment, Northeast Normal University, Changchun 130117, P.R. China. Fax: (+86) 431-89165626; E-mail: guoyh@nenu.edu.cn (Y. Guo)*
[b]*School of Chemistry, Northeast Normal University, Changchun 130024, P.R. China*

‡ Footnotes should appear here. These might include comments relevant to but not central to the matter under discussion, limited experimental and spectral data, and crystallographic data.

1 G. Zhang, G. Kim and W. Y. Choi, *Energy Environ. Sci.* 2014, **7**, 954.
2 H. Tong, S. X. Ouyang, Y. P. Bi, N. Umezawa, M. Oshikiri and J. H. Ye, *Adv. Mater*. 2012, **24**, 229.
3 Y. Q. Qu and X. F. Duan, *Chem. Soc. Rev.* 2013, **42**, 2568.
4 J. X. Xia, S. Yin, H. M. Li, H. Xu, Y. S. Yan and Q. Zhang, *Langmuir*. 2011, **27 (3)**, 1200.
5 G. Liu, L. Z. Wang, H. G. Yang, H. M. Cheng and Gao Qing (Max) Lu, *J. Mater. Chem*. 2010, **20**, 831.
6 J. H. Xu, W. Z. Wang, S. M. Sun and L. Wang, *Appl. Catal. B: Environ*. 2012, **111–112**, 126.
7 R. S. Yuan, T. Chen, E. H. Fei, J. L. Lin, Z. X. Ding, J. L. Long, Z. Z. Zhang, X. Z. Fu, P. Liu, L. Wu and X. X. Wang, *ACS Catal*. 2011, **1**, 200.
8 M. D. Hernández-Alonso, F. Fresno, S. Suáreza and J. M. Coronado, *Energy Environ. Sci.* 2009, **2**, 1231.
9 X. H. Li, J. S. Chen, X. C. Wang, J. H. Sun and M. Antonietti, *J. Am. Chem. Soc.* 2013, **133**, 8074.
10 X. F. Yang, H. Y. Cui, Y. Li, J. L. Qin, R. X. Zhang and H. Tang, *ACS Catal*. 2013, **3**, 363−369.
11 Z. L. Xu, I. Tabata, K. Hirogaki, K. Hisada, T. Wang, S. Wang and T. Hori, *RSC Adv*. 2012, **2**, 103.
12 G. P. Nagabhushana, G. Nagarajub and G. T. Chandrappa, *J. Mater. Chem. A*. 2013, **1,** 388.
13 L. Wang, W. Z. Wang, M. Shang, S. M. Sun, W. Z. Yin, J. Ren and J. Zhou, *J. Mater. Chem. A*. 2010, **20**, 8405.
14 L. Jiang, L. Z. Wang and Ji. L. Zhang, *Chem. Commun.* 2010, **46** , 8067.
15 B. Jiang, P. Zhang, Y. Zhang, L. Wu, H. X. Li, D. Q. Zhang, G. S. Li, *Nanoscale*. 2012, **4**, 455.
16 K. Hemalata Reddy, Satyabadi Martha and K.M. Parida, *RSC Adv*. 2012, **2**, 9423.
17 X. Y. Li, P. Y. Zhang, L. Jin, T. Shao, Z. M. Li and J. J. Cao, *Environ. Sci. Technol*. 2012, **46**, 5528.
18 Z. X. Ji, D. M. Callahan Jr, M. N. Ismail, J. Warzywoda and A. Sacco Jr, *J. Photochem. Photobiol. A: Chem*. 2011, **217**, 22.
19 S. Q. Zhang, L. Chen, H. B. Liu, W. Guo, Y. X. Yang, Y. H. Guo and M. X. Huo, *Chem. Eng. J*. 2012**, 200–202**, 300.
20 E. Taboada, I. Angurell and J. Llorca, *J. Catal*. 2014, **309**, 460.
21 Y. C. Feng, L. Li, J. W. Li, J. F. Wang and L. Liu, *J. Hazard. Mater*. 2011, **192**, 538.
22 Z. H. Ai, W. Ho, S. Lee and L. Z. Zhang, *Environ. Sci. Technol*. 2009, **43**, 4143.
23 Y. F. Fang, Y. P. Huang, J. Yang,P. Wang and G. W. Cheng, *Environ. Sci. Technol*. 2011, **45**, 1953.
24 H. Gnayem and Y. Sasson, *ACS Catal*. 2013, **3**, 186.
25 L. Q. Ye, Y. R. Su, X. L. Jin, H. Q. Xie and C. Zhang, *Environ. Sci. Nano*. 2014, **1**, 90.

26 S. Y. Song, W. Gao, X. Wang, X. Y. Li, D. P. Liu, Y. Xing and H. J. Zhang, *Dalton Trans*. 2012, **41**, 10472.

27 H. F. Cheng, B. B. Huang, P. Wang, Z. Y. Wang, Z. Z. Lou, J. P. Wang, X. Y. Qin, X. Y. Zhang and Y. Dai, *Chem. Commun*. 2011, **47**, 7054.

28 W. Q. Cui, W. J. An, L. Liu, J. S. Hu and Y. H. Liang, *J. Hazard. Mater*. 2014, **280**, 417.

29 G. H. Jiang, R. J. Wang, X. H. Wang, X. G. Xi, R. B. Hu, Y. Zhou, S. Wang, T. Wang and W. X. Chen, *ACS Appl. Mater. Inter*. 2012, **4**, 4440.

30 L. Kong, Z. Jiang, T. C. Xiao, L. F. Lu, M.O. Jonesac and P. P. Edwards, *Chem. Commun*. 2011, **47**, 5512.

31 G. H. Jiang, X. H. Wang, Z. Wei, X. Li, X. G. Xi, R. B. Hu, B. L. Tang, R. J. Wang, S. Wang, T. Wang and W. X. Chen, *J. Mater. Chem. A*. 2013, **1**, 2406.

32 F. Y. Ma, S. Q. Zhang, X. Yang, W. Guo, Y. H. Guo and M. X. Huo, *Catal. Commun*. 2012, **24**, 75.

33 M. Shang,W. Z. Wang and L. Zhang, *J. Hazard. Mater*. 2009, **167**, 803.

34 Y. F. Fang, W. H. Ma, Y. P. Huang and G. W. Cheng, *Chem. Eur. J*. 2013, **19**, 3224.

35 C. L. Yu, K. Yang, Y. Xie, Q. Z. Fan, J. C. Yu, Q. Shu and C. Y. Wang, *Nanoscale*. 2013, **5**, 2142.

36 L. Chen, W. Guo, Y. X. Yang, A. Zhang, S. Q. Zhang, Y. H. Guo and Y. N. Guo, *Phys. Chem. Chem. Phys*. 2013, **15**, 8342.

37 M. H. Su, C. He, L. F. Zhu, Z. J. Sun, C. Shan, Q. Zhang, D. Shu, R. L. Qiu and Y. Xiong, *J. Hazard. Mater*. 2012, **229–230**, 72.

38 L. Zhang, W. Z. Wang, S. M. Sun, Y. Y. Sun, E. P. Gao and Z. J. Zhang, *Appl. Catal. B: Environ*. 2014, **148-149**, 164.

39 W. Guo, Y. X. Yang, Y. N. Guo, Y. Q. Jia, H. B. Liu and Y. H. Guo, *Phys. Chem. Chem. Phys*. 2014, **16**, 2075.

40 X. X. Wei, H. T. Cui, S. Q. Guo, L. F. Zhao and W. Li, *J. Hazard. Mater*. 2013, **263**, 650.

41 X. B. Cao, Z. F. Lu, L. W. Zhu, L. Yang, L. Gu, L. L. Cai and J. Chen, *Nanoscale*. 2014, **6,** 1434.

42 L. Q. Ye, J. Y. Liu, Z. Jiang, T. Y. Peng and L. Zan, *Appl. Catal. B: Environ*. 2013, **142–143**, 1.

Graphical Abstract